Stress state at faults: The influence of rock stiffness contrast, stress orientation, and ratio

Moritz O. Ziegler[1,2], Robin Seithel[3], Thomas Niederhuber[4], Oliver Heidbach[2,5], Thomas Kohl[4], Birgit Mueller[4], Mojtaba Rajabi[6], Karsten Reiter[7], and Luisa Roeckel[4]

[1]Technical University Munich, Arcisstraße 21, 80333 Munich, Germany
[2]Helmholtz Centre Potsdam GFZ German Research Centre for Geosciences, Telegrafenberg, 14473 Potsdam, Germany
[3]GHJ - Ingenieurgesellschaft für Geo- und Umwelttechnik mbH & Co. KG, Am Hubengut 4, 76149 Karlsruhe, Germany
[4]Institute of Applied Geosciences, KIT, 76131 Karlsruhe, Germany
[5]Institute for Applied Geosciences, TU Berlin, 10587 Berlin, Germany
[6]School of the Environment, University of Queensland, 4072 Saint Lucia, Queensland, Australia
[7]Institute of Applied Geosciences, TU Darmstadt, 64287 Darmstadt, Germany

Correspondence: Moritz O. Ziegler (moritz.ziegler@tum.de)

Abstract. The contemporary crustal stress state is primarily driven by gravitational volume forces and plate tectonics. However, there are various smaller scale sources such as geological structures and stiffness contrast that perturb stresses and deviate them from the regional pattern. For example, borehole stress analysis in numerous cases, has revealed abrupt rotations of horizontal stress orientation of up to 90° when faults are crossed. Herein, we investigate the rotation of principal stress axes at a fault by means of a 2D generic numerical model. We focus on the near field of the fault and the damage zone with a fault parameterised as a rock stiffness contrast. A substantial influence of the far field stress field in terms of the differential stress and in terms of the stress ratio $R_S = S_1/S_3$ is shown. Furthermore, the contrast in material properties is the basis for any stress rotation and in particular the stiffness is demonstrated to have a significant influence. Eventually, the impact of the angle between the fault strike and the orientation of S_{Hmax} is demonstrated. Our results show that the stress rotation is negatively correlated with the ratio of principal far-field stresses. A small angle between the far-field stress orientation and the fault facilitates stress rotation. A high contrast in rock stiffness further increases the stress rotation angle. Faults striking perpendicular to the maximum principal stress orientation experience no rotation at all. However, faults oriented parallel to the maximum principal stress orientation experience either no rotation or a 90° rotation, dependent on the ratio of principal stresses and the rock stiffness contrast. A comparison with observations from various boreholes worldwide shows that in general, the findings are well in agreement, even though the dip angle proves to have an influence on the stress rotation, in particular for shallow dipping faults.

1 Introduction

The contemporary crustal stress state is a key parameter in the stability and safety assessment of subsurface operations, such as the extraction of raw materials, storage of waste and exploitation of geothermal energy (Catalli et al., 2013; Müller et al., 2018; van Wees et al., 2018). Most frequently freely available and most easily obtained stress information is the orientation

1

of the maximum horizontal stress component S_{Hmax} which is compiled in the World Stress Map (Heidbach et al., 2018). Often, the S_{Hmax} orientation is observed to be consistent over large areas and volumes following the general patterns imposed by plate tectonics (Han et al., 2019; Heidbach et al., 2018; Engelder, 1992; Rajabi et al., 2017a; Reiter et al., 2014), but regionally variable patterns are also observed (Konstantinou et al., 2017; Niederhuber et al., 2023; Ziegler et al., 2016c). The
25   S_{Hmax} orientation pattern is influenced by topography of large mountain ranges (Levi et al., 2019; Reinecker et al., 2010; Zoback, 1992; Engelder, 1992) or sedimentary basin geology (Rajabi et al., 2016a, b; Snee and Zoback, 2018). It has also been hypothesized that the S_{Hmax} orientation is diverted by faults (Dart and Swolfs, 1992; Faulkner et al., 2006; Konstantinovskaya et al., 2012; Li et al., 2023; Schoenball et al., 2018; Yale, 2003). Reiter et al. (2024) showed with a comprehensive study using a generic geomechancial model that large-scale fault induced stress changes due to a discontinuity beyond a distance of a few
30   hundred meters from the fault core are too small to be resolved by stress data.

     Nevertheless, on a meter scale in boreholes abrupt or gradual rotations of the S_{Hmax} orientation have been observed (Barton and Zoback, 1994; Brudy et al., 1997; Massiot et al., 2019; Sahara et al., 2014; Shamir and Zoback, 1992; Wang et al., 2023). Over the last decade, a great increase in high-resolution image logs in various basins, provides the opportunity for detailed observation of such small-scale stress rotations in the vicinity of faults at borehole scales (Lin et al., 2010; Rajabi et al.,
35   2022, 2024; Sahara et al., 2014; Talukdar et al., 2022; Zhang et al., 2023). Figure 1a shows an example of stress re-orientation of approximately 90° indicated by borehole breakouts (Bell and Gough, 1979; Heidbach et al., 2018; Engelder, 1992) in the vicinity of and attributed to a fault, which has been interpreted in an electrical image log in the Surat Basin of Queensland, Australia (Rajabi et al., 2017a).

     The observed change in breakout orientation is the manifestation of a change in the orientation of the maximum circum-
40   ferential stress at the borehole wall (Figure 1b) which is a function of the position at the borehole wall with respect to the orientation of the principal stresses components S_1, S_2, and S_3 (Kirsch, 1898). The principal stress components result from the transformation of the 2nd order symmetric stress tensor

$$\sigma_{ij} = \begin{pmatrix} \sigma_{xx} & \sigma_{yx} & \sigma_{zx} \\ \sigma_{xy} & \sigma_{yy} & \sigma_{zy} \\ \sigma_{xz} & \sigma_{yz} & \sigma_{zz} \end{pmatrix} \tag{1}$$

into the main axis system (2), where the three remaining components are the three principal stresses that are perpendicular
45   to each other, and it is defined that $S_1 > S_2 > S_3$.

$$\sigma = \begin{pmatrix} S_1 & 0 & 0 \\ 0 & S_2 & 0 \\ 0 & 0 & S_3 \end{pmatrix} \tag{2}$$

     Any changes in the magnitudes of the individual components of the stress tensor σ_{ij} are reflected in the principal stress components. In the main axis system, the changes in magnitudes in σ_{ij} can also be reflected by changes in principal stress

axis orientation (Figure 1b) However, this only occurs if the deviatoric stress tensor changes (Engelder, 1994). In general, the phenomenon of changes in the magnitudes of the components of σ_{ij} that can be observed as changes in the orientation of the principal stress axes and is commonly referred to as stress rotation. It can be observed e.g., as a change in the orientation of borehole breakouts (Figure 1a).

Stress rotations are observed at various locations worldwide where boreholes have been drilled through faults while observations of the stress state were possible (e.g., Brudy et al., 1997; Cui et al., 2014; Hickman and Zoback, 2004; Lin et al., 2007). While some faults exhibit a rotation of up to 90° (Lin et al., 2007), others show significantly less (Cui et al., 2014; Hickman and Zoback, 2004) or considering the uncertainties almost no rotation at all (Yamada and Shibanuma, 2015). Even though stress rotations can be observed in boreholes under some circumstances, knowledge of where to expect stress rotations is important for subsurface operations that specifically target faults for their permeable properties (Freymark et al., 2019; Konrad et al., 2021) or may avoid them for the same reasons but still will encounter them (Gilmore et al., 2022; Long and Ewing, 2004). This raises the questions as to which parameters determine a stress rotation and how sensitive they are.

The potential for stress rotation and the magnitude for such rotation are assumed to be determined by the smallest and largest principal stress components S_1 and S_3, usually considered in terms of the differential stress S_1-S_3 (Reiter, 2021; Sonder, 1990; Ziegler et al., 2017), the contrast in rock stiffness between the fault and an intact host rock, and the angle of the fault strike represented by a rock stiffness contrast with respect to the orientation of S_{Hmax} (Reiter, 2021; Siler, 2023). Several additional parameters such as rock fabric and geological structures (i.e., faults and fractures) have been suggested as the possible causes of these stress re-orientations at small scales (Faulkner et al., 2006; Hung et al., 2007; Siler, 2023; Yale, 2003).

We investigate the reason for the diverse behaviour of the stress state at faults from a geomechanical perspective and investigate the influence of various parameters on the angle of stress rotation. We focus on the near field of the fault and the damage zone, i.e., the volume around the fault where the rock is significantly fractured and affected in its integrity. We expect a substantial influence of the far field stress field in terms of the differential stress as shown in previous studies (Reiter, 2021; Sonder, 1990; Ziegler et al., 2017) but also in terms of the stress ratio R_S=S_1/S_3. Furthermore, the contrast in material properties is the basis for any stress rotation and in particular the stiffness (Young's modulus) is demonstrated to have a significant influence (Hergert et al., 2015; Reiter, 2021; Ziegler, 2022). Eventually, the angle between the fault strike and the orientation of S_{Hmax} is investigated as an influential parameter (Reiter et al., 2024; Siler, 2023).

We use a generic geomechanical-numerical model that allows a systematic and comprehensive investigation of the model parameter space in terms of stiffness contrast, stress ratio, and angle of the fault with respect to the far field stress state. We focus on the near field of the fault at scales of 10s of meters and limit the investigation to the linear elastic response of the stress state to rock stiffness contrasts which has not been investigated in previous studies that focused on processes (Ziegler et al., 2017), did not investigate the full range of parameters (Reiter, 2021) and methods of fault representation due to a different objective (Reiter et al., 2024). Herein, we conduct an exhaustive study and investigate the entire parameter space.
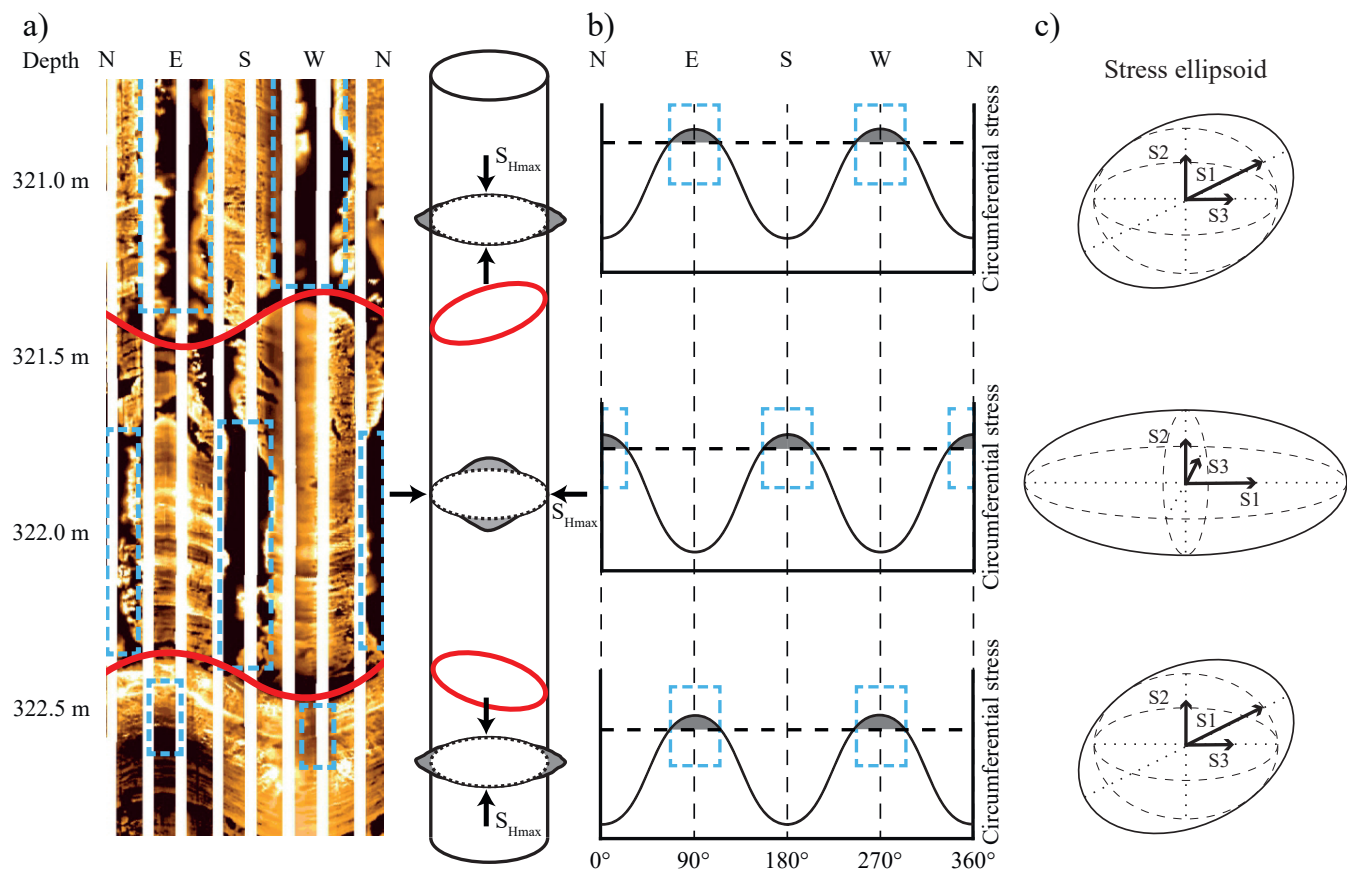
3

Figure 1. An example of stress rotation due to the presence of a small-scale fault in a borehole. The regional S_{Hmax} orientation in the vicinity of this well is approx. 0° (Rajabi et al., 2017a) as indicated by borehole breakouts (black areas in image log) oriented East-West above and below the fault zone delineated by the two sinusoidal red lines. The part in between shows the section that is affected by the fault and thus shows a rotated stress state. a) Borehole breakouts (blue dashed lines) interpreted in a resistivity image log in the Kenya East Well in the Surat Basin, Eastern Australia and the borehole diameter represented in 3D. Dark areas represent conductive zones where the borehole is elongated and light areas zones of high resistivity. b) Variations of the circumferential stress at the borehole wall (bold sinusoidal line) with the orientations where the compressive strength (dashed horizontal line) is exceeded (grey areas) and breakouts occur (dashed blue lines). c) Representation of the stress tensor above and below the fault with the stress ellipsoid visualizing orientations and magnitudes of the three principal stresses S_1, S_2, and S_3.

2 Model setup

In order to investigate the stress rotation at a fault dominated by mode-II-failure (shear failure) we set up a numerical 2D plane strain model that focuses on the basic characteristics of a material contrast at faults. A generic mature fault zone is assumed with no damage zone outside the core and highly localized damage represented by a 5m wide zone with a reduction in stiffness. The model assumes a vertical fault in a strike slip stress regime in map view, i.e., the largest principal stress component $S_1=S_{Hmax}$

4

and the smallest principal stress component is S_2 due to the limitation to two dimensions and is assumed to be S_{hmin}. At the same time, the model is also representative for other types of faults which requires to assume the model to be a depth section. For a normal fault $S_1=S_v$ and $S_2=S_{hmin}$ or for a thrust fault $S_1=S_{Hmax}$ and $S_2=S_v$.

The dimension of the numerical model is 10 x 10 km^2 with a central 5 m wide fault that dissects the entire model (Figure 2a). We use the finite element method to solve the problem numerically and the model is discretized in a way that boundary effects and numerical artefacts are reduced (Homberg et al., 1997; Spann et al., 1994). Within the fault, plane strain quad-elements form a finite element mesh with a resolution of 5 m along strike and 0.25 m normal to the fault strike. These elements represent the fault by a rock stiffness that is different to that of the host rock. The 200 m at each side of the fault are also discretized by quad-elements (Figure 2c). The element size normal to the fault strike increases with distance from the fault. Outside the immediate vicinity of the fault, plane strain tria-elements with a mesh coarsening to 100 m at the boundary are used (Figure 2b). In total 19 realizations of the model were created with different strike angles of the fault. The number of elements slightly varies depending on the strike angle but is always between 145,612 and 172,484 elements. An exception is made for a high resolution model (732,526 elements) for visualization purposes with a fault strike angle of 15°. The independence of the solution from the discretization is shown in Appendix A. The stress state of the model is controlled with displacement boundary that are chosen in such a way that they result in the desired horizontal stress magnitudes (Figure. 2a)(Ziegler et al., 2023).

To evaluate which parameter controls the amount of stress rotation, we systematically vary the stiffness contrast between the fault and the host rock, the ratio of principal stresses $R_S=S_1/S_2$, and the angle γ between the faults strike and the far-field S_1 orientation (Table 1). For the host rock we choose a Young's modulus $E_{host}=40$ GPa and a Poisson's ratio of 0.25 and for the fault, the stiffness is systematically varied between $E_{fault}=0.4$ GPa and $E_{fault}=40$ GPa, resulting in 13 scenarios with a rock stiffness contrast $R_E=E_{fault}/E_{host}$ between 0.01 and 1. This corresponds to a range from a very soft fault up to the intact rock. The Poisson's ratio was kept constant at 0.25 as the influence of the stiffness is considered as the most important parameter, as shown by previous studies (Reiter, 2021; Ziegler, 2022). We tested the influence of the material contrast in eleven far field principal stress ratios. We iterated the angle γ from 0° to 90° in 5°-steps. For the full parameter space this results in total in 2717 model scenarios that were solved and then analysed.

Table 1. Range of parameters investigated in this study. Note that the rock stiffness contrast R_E has a step width of 0.1 (4 GPa) between a R_E=1 and R_E=0.1. Larger contrasts are realised to be 0.07, 0.04, and 0.01. The host rock always has a Young's modulus of E_{host}=40 GPa. The stress ratio Rs, the differential stress S_1-S_2, and the absolute stress magnitudes are indicated. γ is the angle between fault strike and S_1 orientation that varies between $0°$ (parallel) and $90°$ (perpendicular). The results of all computations are provided in the supplementary material.

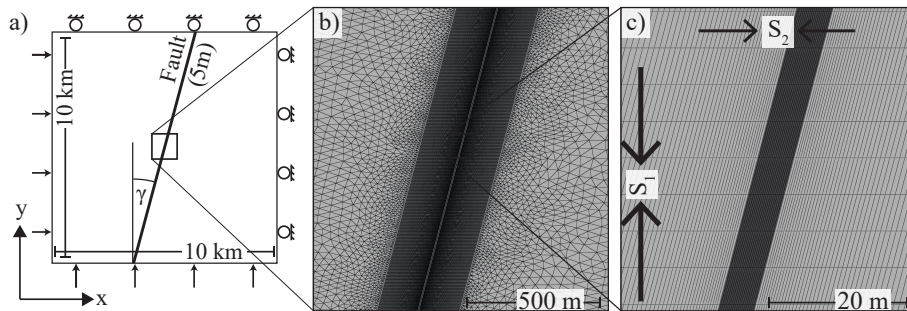| Parameter	Values																		Num. scen.
R_E	1	0.9	0.8	0.7	0.6	0.5	0.4	0.3	0.2	0.1	0.07	0.04	0.01						13
E_{fault} [GPa]	40	36	32	28	24	20	16	12	8	4	2.8	1.6	0.4						
$R_S=S_1/S_2$	1.0	1.1	1.2	1.3	1.4	1.5	1.6	1.7	1.8	1.9	2.0								11
S_1-S_2 [MPa]	0.00	2.25	5.00	8.25	12.00	16.25	21.00	26.25	32.00	38.25	45.00								
S_1 [MPa]	20.00	24.75	30.00	35.75	42.00	48.75	56.00	63.75	72.00	80.75	90.00								
S_2 [MPa]	20.0	22.5	25.0	27.5	30.0	32.5	35.0	37.5	40.0	42.5	45.0								
γ [°]	0	5	10	15	20	25	30	35	40	45	50	55	60	65	70	75	80	85	90 — 19

Figure 2. Sketch of the model setup. a) Conceptual setup of the generic 2D model with the applied boundary conditions and the location of the fault in the centre of the model. Please note that the fault can be rotated in $5°$ steps. b) Detailed excerpt that shows the refined mesh geometry in the fault core and close to the fault. An area of 200 m on either side of the fault is discretised with quadrilateral elements for a better resolution. c) Closeup of the fault (dark area) and its immediate vicinity (light area) that shows the high resolution of 25 cm normal to the fault strike and 5 m in fault strike direction. Please not that S_1=S_{Hmax} and S_2=S_{hmin}.

3 Results

The rotation of the principal stress axes at a material contrast in a fault centre are investigated. In a sensitivity study, the influence on the rotation of (1) the material contrast ratio, (2) the initial stress ratio, and (3) the orientation between the faults strike and the background stress field orientation are tested. A 2D geomechanical-numerical finite element model is used to rapidly solve various scenarios which are analysed in the following.

The models provide at the nodes of the finite elements the normal stress components σ_{xx} and σ_{yy} and the shear stress component σ_{xy}. The orientation of S_1 in the far-field from the fault is parallel to the y-axis (Figure 2c). In order to obtain the angle of stress rotation we determine the change of the S_1 and S_2 orientation in the centre of the fault with the initial far-field orientation. The influence of the three individual parameters on the stress rotation angle is investigated in a sensitivity study in the following.

3.1 Basic behaviour

The difference between far-field stress state and the altered stress state due to the material contrast are displayed in Figure 3. In order to initially test the hypothesis that the three parameters, the angle γ between the faults strike and the background stress field, the rock stiffness contrast R_E, and the relative stress magnitudes of S_1 and S_2 influence the stress rotation angle, each of the parameters is changed and the results are observed in the individual panels of Figure 3 in comparison to Figure 3a.

The stress rotation for a fault with an angle $\gamma = 15°$ between the strike of the fault and the orientation of the far-field stress component (S_1), a moderate stiffness contrast R_E=0.4 (16 GPa fault, 40 GPa host rock), and a principal stress ratio R_S=1.4 ($S_1 = 35$ MPa, $S_2 = 25$ MPa, S_1-$S_2 = 10$ MPa) is displayed in Figure 3a. A clockwise rotation of the principal stress axes by 59° can be observed in the fault centre. Outside this zone, the principal stress orientations adhere to the far field stress state as no visual rotation can be observed (Figure 3a). This setting is used as a reference and compared to changes due to altered individual parameters in the following. The results are displayed in Figure 3 and summarized in Table 2.

A decrease of the stress ratio to R_S=1.2 while the differential stress S_1-S_2 remains constant (but the magnitudes of the principal stresses change to $S_1 = 60$ MPa and $S_2 = 50$ MPa) leads to an increased stress rotation angle of 68° (Figure 3b). An increase in S_1-S_2 from 10 MPa to 30 MPa ($S_1 = 105$ MPa, $S_2 = 75$ MPa) while R_S=1.4 and therefore constant results in the same rotation angle of 59° as in the reference case (Figure 3c). In contrast, an increase in S_1-S_2 to 30 MPa ($S_1 = 70$ MPa, $S_2 = 40$ MPa) with a change in stress ratio to R_S=1.75 results in a decrease of stress rotation to 45° (Figure 3d). This indicates that it is rather the stress ratio R_S that controls the stress rotation than the differential stress S_1-S_2. A more comprehensive comparison is shown in Table 3 which indicates the independence of stress rotation angle from differential stress S_1-S_2 and its dependence on stress ratio R_S.

A reduction of the stiffness contrast from R_E=0.4 to R_E=0.7 means that the fault is stiffer and thus closer to the host rocks stiffness. This results in a reduction of the stress rotation of 31° to 28° (Figure 3e). This positive correlation of rock stiffness contrast R_E to potential stress rotation angle has been observed previously (Reiter, 2021). It is intuitive in that with the herein

7

made assumptions the same stiffness in fault and host rock (R_E=1) cannot lead to any rotation at all. Thus, greater stiffness contrast (small values for R_E) promote less stress rotation.

145   An increase in the angle γ between the fault strike and the far-field S_1 orientation from initially 15° to now 45° results in a smaller rotation angle of 19° (Figure 3f). The angle γ is thus negatively correlated with the rotation angle. No rotation is expected for faults that strike perpendicular to the S_1 orientation (γ=90°). Large stress rotation angles are expected for faults that strike with a low angle towards the S_1 orientation.

3.2   Spatial effects

150 As already indicated in Figure 3, stress rotation is observed only directly in the fault zone where a rock stiffness contrast R_E exists. In order to investigate its influence beyond the fault itself we display the stress rotation angle as a function of distance normal to the fault (Figure 4). In this idealized representation of a fault without a damage zone, no significant changes in the orientation of S_1 can be observed outside the fault (Figure 4). However, significantly different stress rotation angles are observed within the fault dependent on the R_E value in line with the observations made in Figure 3b and e.

155   Furthermore, within the contrasting rock volumes there is no gradual difference observed between the borders and the centre (Figure 4). Only at the border between fault and host rock, an intermediate stress rotation angle can be observed (transition from grey to white in Figure 4). This apparent stress rotation should not be interpreted as it is a result of the interpolation from the integration points within the elements to the nodes. At the borders between bodies with different material properties the stress state is a mixture of stress states from the two bounding lithologies and its extent depends on the discretization. It can be

160 disregarded in the following analysis. Thus, in the following we refer to the stress rotation in the centre of the modelled fault only. This allows to display the results in a more comprehensive way (Figure 5).

3.3   Parameter space

In order to explore the full parameter space, we chose a different visualization. Each stress ratio R_S is represented by an individual diagram (panels of Figure 5). Within each diagram, the angle γ between fault strike and S_1 orientation is related to

165 the modelled stress rotation angle. Each model scenario with an individual set of parameters is now displayed as a point in a diagram (Figure 5). The material contrast R_E is colour-coded. Four different stress ratios R_S are compared in the four panels of Figure 5.

    The initial observation is the importance of the angle γ. Structures with a significant contrast in rock stiffness that are perpendicular to the far field orientation of S_1 (γ=90°) do not exhibit any rotation of the principal stress axes at all. This

170 is independent of all other parameters. In turn, structures parallel to the S_1 orientation (γ=0°) can rotate by up to 90°. This signifies a mutual replacement of S_1 and S_2 orientation. Whether a stress rotation of 90° is reached or not is tied to the ratios R_E and R_S.

    For large contrasts (i.e. small R_E) and small R_S values, the maximum stress rotation angle is reached in several scenarios. At the same time, high R_E values limit the maximally achieved stress rotation angle. The maximum angle for any given R_E value

175 is then up to 90° and controlled by the stress ratio R_S (Figure 5). However, in these cases the maximum angle is not observed

Table 2. All parameters of the model scenarios tested in Figure 3 listed according to the panels.

Panel	R_S	S_1-S_2	S_1	S_2	R_E	γ	Rotation
a	1.4	10 MPa	35 MPa	25 MPa	0.4	15°	59°
b	1.2	10 MPa	60 MPa	50 MPa	0.4	15°	68°
c	1.4	30 MPa	105 MPa	75 MPa	0.4	15°	59°
d	1.75	30 MPa	70 MPa	40 MPa	0.4	15°	45°
e	1.4	10 MPa	35 MPa	25 MPa	0.7	15°	28°
f	1.4	10 MPa	35 MPa	25 MPa	0.4	45°	20°

for $\gamma=0°$ but for angles $0° < \gamma < 45°$. Apparently, for an angle $\gamma = 0°$ either no stress rotation at all or the maximally possible stress rotation of 90° occurs.

The large influence of the R_S value is additionally displayed in a representation of the three model parameters investigated in this study where the decisiveness of the R_S value becomes apparent (Figure 6). This is in particular observable for $R_E=0.6$ at faults that are striking parallel to the S_1 orientation ($\gamma=0°$). A low R_S of around 1.1 leads to a stress rotation of 90° (Figure 5a). However, an increase of R_S to ≥ 1.5 (Figure 6) prevents any stress rotation at all.

These results show, that the previously indicated correlations (Figure 3) can be confirmed. These are in particular:

- A negative correlation between R_S and the stress rotation angle, i.e. large stress rotations for principal stress magnitudes that are similar to each other.

- A negative correlation between R_E and the stress rotation angle, i.e. large stress rotations for large material contrast (small values of R_E).

- A mostly negative correlation between the angle γ between strike angle vs. far-field S_1 orientation and the stress rotation angle, i.e. S_1 which acts normal to a faults strike will see no rotation. An exception is a angle of $\gamma=0°$ where either no stress rotation or a rotation of 90° is observed.

This shows the combined influence of the stress ratio, the magnitude of material contrast, and the orientation of the fault strike compared to the far-field stress state on the angle of stress rotation. The expected angle of stress rotation can be estimated if all corresponding data is available.

In addition to the previously mentioned correlations, further rules can be observed in Figure 5. The sum of the angle between fault strike and far-field stress orientation γ and the angle of observed stress rotation cannot exceed 90°. No rotation is observed if the fault strikes perpendicular to the far-field stress orientation, i.e. $\gamma=90°$. A rotation of 90° is only possible if $\gamma = 0°$. However, not for all scenarios with $\gamma = 0°$ a rotation of 90° is observed. Whether any rotation is observed or not depends on the stiffness contrast. This highlights the importance of all three parameters on the expected angle of stress rotation.

Table 3. Dependence of the stress rotation on the stress ratio R_S. The R_S values are compared with different S_1-S_2 associated with the same angle $\gamma=15°$ and the same rock stiffness contrast $R_E=0.4$.

	$R_S = 1.2$		
S_1-S_2 [MPa]	6	10	14
Stress rotation [°]	67.7	67.7	67.7
	$R_S = 1.4$		
S_1-S_2 [MPa]	12	14	18
Stress rotation [°]	59.1	59.1	59.1
	$R_S = 1.6$		
S_1-S_2 [MPa]	18	30	42
Stress rotation [°]	50.5	50.5	50.5
	$R_S = 1.8$		
S_1-S_2 [MPa]	24	40	56
Stress rotation [°]	43.1	43.1	43.1
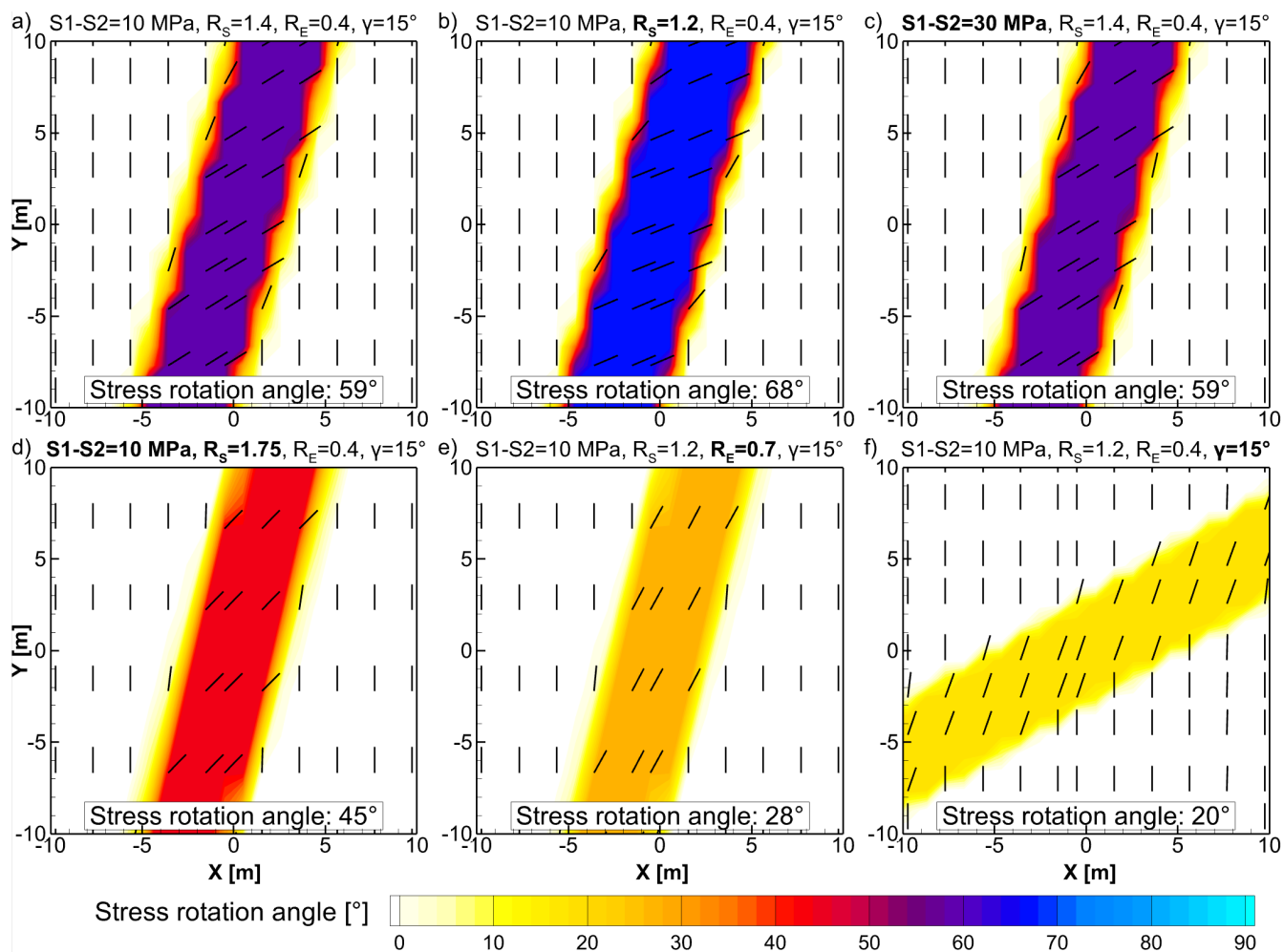
Figure 3. Influence of different parameters on the stress rotation angle. The stress rotation colour-coded and as vectors/lines that indicate the S_1 orientation due to a material contrast in the fault core area (Figure 2c). a) A basic setting with a fault that is 15° deviated from the orientation of S_1, a differential stress of 10 MPa, a stress ratio of R_S=1.4, and a rock stiffness contrast of R_E=0.4 (E=16 GPa in the fault core and E=40 GPa in the host rock. This reference setting is compared with stress rotation based on individually changed parameters (bold in titles of b – f). b) R_S=1.2. c) Differential stress increased to 30 MPa and R_S =1.2. d) Differential stress increased to 30 MPa with the same S_2 magnitude as in a), R_S=1.75. e) R_E=0.7. f) Deviation of 45° between fault strike and the S_1 orientation. All panels parameters are comprehensively listed in Table 2.
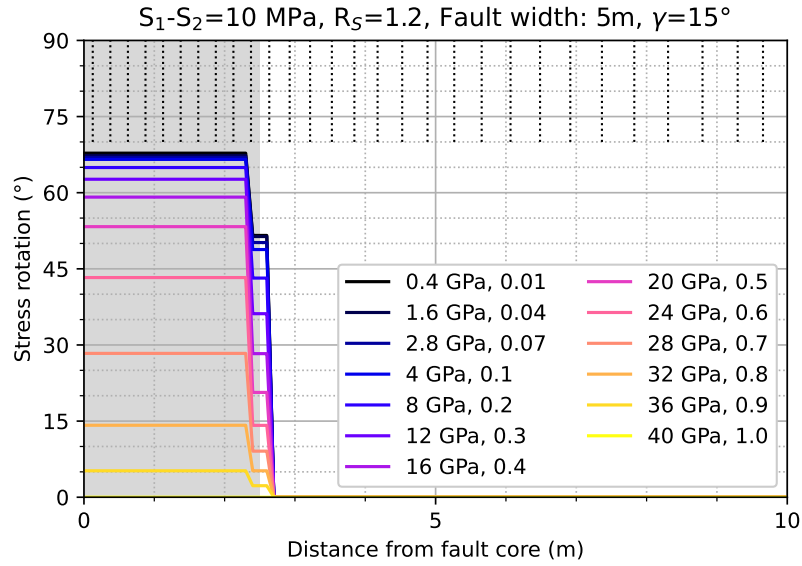
Figure 4. Intrinsic stress rotation in the fault zone as a function of increasing rock stiffness contrast. The abrupt change from a rotated to a far-field stress state is observed at the border of the fault. The rotation is shown perpendicular to the fault. The rock stiffness contrast between the fault's Young's modulus and a host rock stiffness of E_{host}=40 GPa is colour-coded and indicated in the legend as absolute values in GPa and ratio R_E. For reference: Purple line R_E=0.4 is taken from Figure 3a; Orange line R_E=0.7 is taken from Figure 3e. See also Table 2 The distance from the fault core centre (x-axis) in relation to the stress rotation (y-axis). The vertical dotted lines at the top indicate the discretization normal to the fault strike with an element size of 25 cm within the fault and increasing outside the fault. Please note, that the distance is from the fault core centre, thus only half of the fault width is shown here in grey.
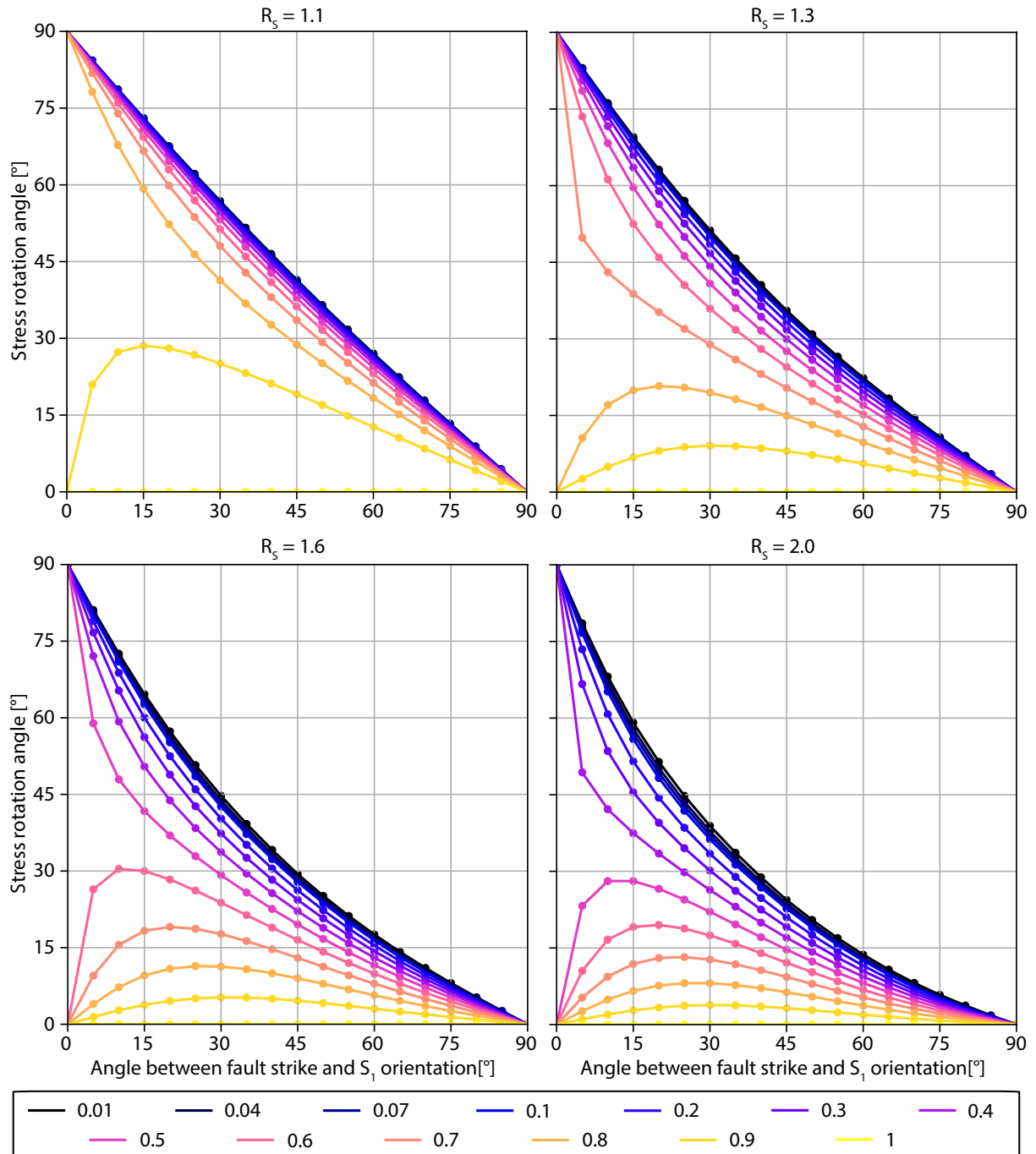
Figure 5. The dependence of stress rotation inside the fault core (y-axes) on the angle γ between the fault strike and the far-field orientation of S_1 (x-axes), the stiffness contrast R_E between fault core and host rock (colour coded lines), and the stress ratio R_S (panels). The underlying data is provided in the supplementary material.
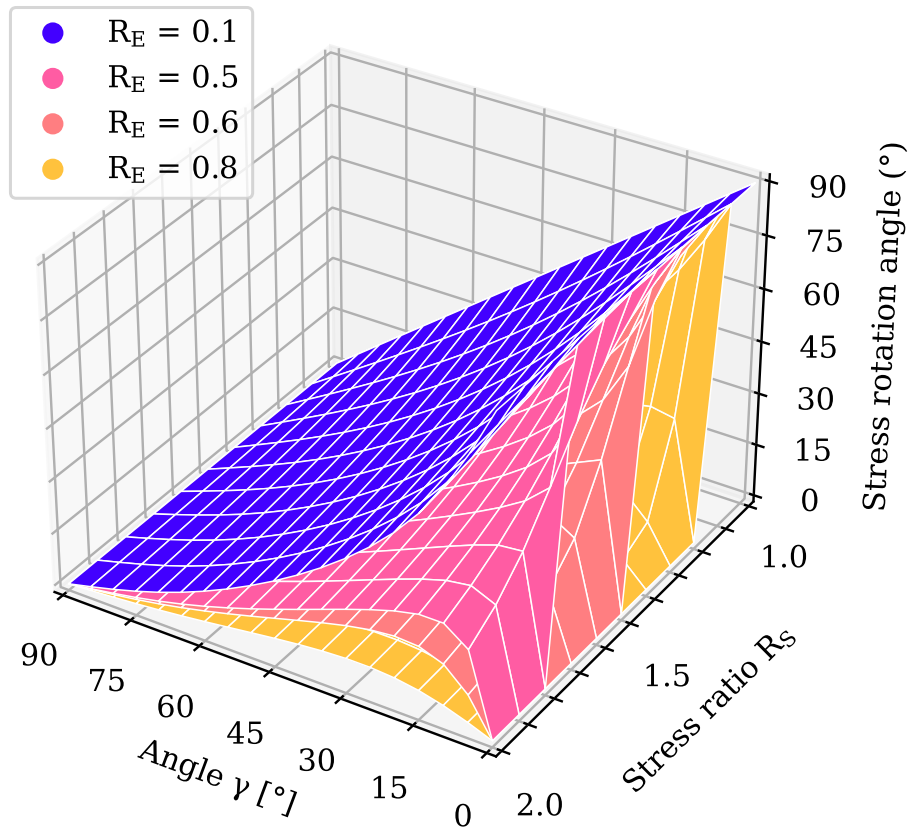
Figure 6. 3D representation of the stress rotation (z-axis) and its dependecy on the stiffness contrast R_E (color-coded planes), angle γ between fault and S_1 orientation (x-axis), and the stress ratio R_S (y-axis). To improve visibility only four different R_E are displayed.

4 Discussion

The influence of the rock stiffness contrast R_E, the stress ratio R_S, and angle between a fault or in general a geological structure and the far-field S_1 orientation on the rotation of the principal stress axes are derived from a generic study using a 2D plane strain numerical model. The results indicate the importance of the aforementioned parameters on the possibility for occurrence and expected angle of stress rotation. They are discussed in light of their general geological implications, the impact on geoenergy applications, and their limitations.

4.1 Implication for fault zones

Faults and fault zones are diverse in their extent, characteristics and behaviour (Gabrielsen et al., 2017; Childs et al., 2009). While they have several characteristics in common, other features may vary greatly. For example, for some faults a significant damage zone is expected around the fault core which largely depends on the faults maturity (Gabrielsen et al., 2017; Childs et al., 2009). Furthermore, the dominant processes that control fault zone behaviour differs which highlights the complexity to geomechanically describe a fault zone.

For the presented study, we assume a weakened fault core compared to the host rock (Casey, 1980; Faulkner et al., 2006, 2010; Isaacs et al., 2008; Holdsworth, 2004; Collettini et al., 2009). The weakness of fault material is herein implemented as a reduced Young's modulus focused on the fault core assuming a mature fault zone with a clearly delineated core and localized damage. Such a sharp elastic stiffness contrast between the host rock and the fault core is observed for some fault zones in nature (Barton and Zoback, 1994; Holdsworth et al., 2010). Other (less mature) fault zones have several meters (Barton and Zoback, 1994; Lockner et al., 2009) or even several tens of meters (Faulkner et al., 2006, 2010; Li et al., 2012; Williams et al., 2016) of damage zone, which separates the intact rock from the fault core.

To investigate the influence of a significant damage zone as assumed for an immature fault zone, a gradual change in rock properties is implemented in an additional model. Therefore, a linear gradient in rock stiffness perpendicular to the fault strike increases the Young's modulus from the faults stiffness to the host rocks stiffness. The resulting stress rotation display a gradual decrease from the fault core towards the intact host rock (Figure 7). The angles observed within the damage zone correspond to those observed for the same rock stiffness within the fault core from previous model results (Figure 5). They do not show any particular deviations from the previously modelled correlations. It is particularly noteworthy, that the non-linear dependency on the rock stiffness contrast is reflected in the gradual decrease in stress rotation from the fault core through the damage zone towards the intact host rock.

This shows that the extent of a deviated stress field around a structure with different rock stiffness is dependent on the transition from host rock properties to deviated rock properties. This means that in this simple, generic case the different rock properties in the structure itself are not having any influence on the stress rotation angle beyond its border. Any modelling approach that chooses a representation of faults by a weakened rock material has to include the damage zone – if it is observed and its extent known – in terms of rock properties.
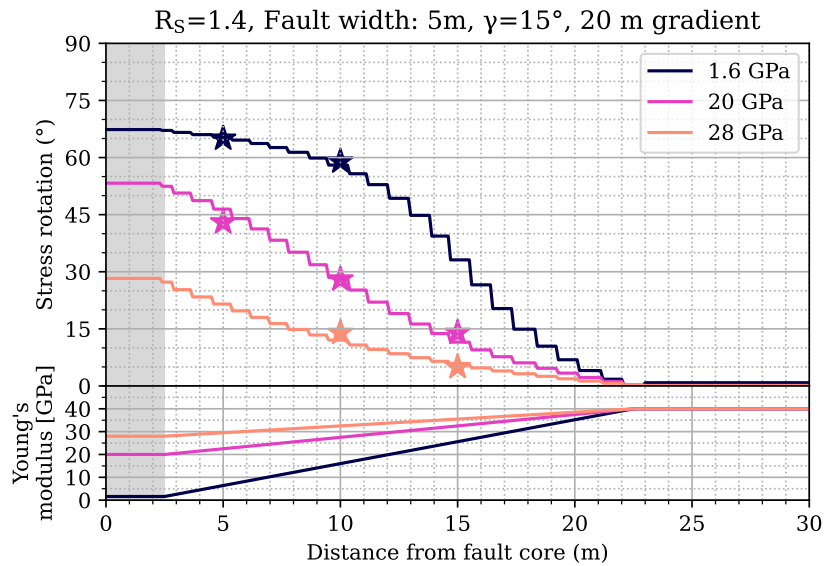
Figure 7. Stress rotation in the vicinity of a fault (top) with different fault stiffness (colour coded lines) in contrast to the same host rock stiffness of 40 GPa with a stress ratio $R_S=1.4$ and an angle $\gamma=15°$. The damage zone of the fault is realised by an increase of stiffness over 20 m (bottom). The stress rotation angles expected according to the presented study (Figure 5) without a gradient of rock stiffness are indicated (stars).

4.2 Application

Modelling of the behaviour of a stiffness contrast with regards to stress rotation is of particular interest for geotechnical ventures. The occurrence of stress rotation is particularly significant for applications such as geothermal energy, where often faults are specifically targeted for their permeability (Barton et al., 1995; Konrad et al., 2021; Seithel et al., 2015; Siler, 2023). At the same time, these faults potentially host induced seismicity (Gaucher et al., 2015; Schoenball et al., 2014; Seithel et al., 2019). Further geotechnical operations, such as mining and tunnelling, affect the stress state, weaken the rock and lead to stress rotations themselves (Cai et al., 2022; Ptáček et al., 2015; Ziegler et al., 2015) which can lead to rockfall or other damages. Thus, it is of key interest to estimate the potential for these damages such as (induced) seismicity on pre-existing faults in advance.

This requires detailed information on the stress state itself but also the angle of faults with respect to the stress state is crucial (Healy and Hicks, 2022; Morris et al., 1996; Röckel et al., 2022; Worum et al., 2004). Often, a regional stress state obtained from geomechanical models does not include local fault geometries (Ahlers et al., 2022; Clavijo et al., 2024; Gradmann et al., 2024). Then, the modelled stress state is mapped to fault geometries and the according potential for failure is estimated (Röckel et al., 2022; Vadacca et al., 2021; Ziegler et al., 2016a, b). In other instances, faults and their effect on the stress field are included in the model (Hergert et al., 2015; Wees et al., 2003; Xing et al., 2007).

245 Various different approaches to include faults in a model exist which mimic the different involved processes that have a different impact on the fault behaviour (Henk, 2020; Reiter et al., 2024; Treffeisen and Henk, 2020; Cappa and Rutqvist, 2011). As a result, faults represented in numerical models tend to be implemented in different ways depending on the focus of a study (Henk, 2020; Reiter et al., 2024). Instead of aiming at a realistic representation of a fault, different aspects of a faults properties are commonly investigated individually. This can be the slip behaviour (Hergert et al., 2015; Reiter et al., 2024),

250 the plastic deformation (Nabavi et al., 2018), or the approach presented in this study as the alteration of rock properties in the immediate fault core and damage zone (Reiter et al., 2024; Treffeisen and Henk, 2020; Cappa and Rutqvist, 2011).

This bears the potential that the reactivation potential of a fault is incorrectly estimated if the stress state inside a fault zone is not or not correctly modelled. This can happen if the far-field stress state is assumed to be the correct stress state inside a fault instead of a rotated far-field stress state. Röckel et al. (2022) potentially indicate this challenge which in some regions could

255 contribute to a mismatch of estimated slip tendency and observed seismicity. Consequently, wrong estimates of the potential for seismicity could be provided by geomechanical models. Knowledge of the expected stress rotation as a result of the setting provide a first indication on whether significant rotations of the principal stress axes are expected or not.

4.3   Observations

Rotations of the S_{Hmax} orientation associated with changes in rock stiffness are mainly observed in boreholes, e.g. by rotating

260 borehole breakouts or drilling induced tensile fractures (Brudy et al., 1997; Cui et al., 2014; Haimson et al., 2010; Hickman and Zoback, 2004; Lin et al., 2007; Massiot et al., 2019). Some notable examples are shown in Table 4. The observation is inherently subject to uncertainties due to the need for breakouts or drilling induced tensile fractures to occur in order to be able to identify a rotation. Thus, the number of significant observations of rotations is rather small and for some projects no rotation at the fault can be observed (Brodsky et al., 2017). In the following we use the investigated correlations to link an observed

265 stress rotation to a stiffness contrast. Therefore, we use available estimates on the stress ratio and observations of a fault in conjunction with the far-field stress orientation.

Massiot et al. (2019) observed significant rotations of the S_{Hmax} orientation in the Taranaki Basin offshore New Zealand. Most prominently a 30° rotation at the intersection of the borehole Whio-1 with the almost vertically dipping Whio-1-fault. In this setting the orientation of S_{Hmax} is approximately parallel to the strike of aforementioned fault (Massiot et al., 2019;

270 Rajabi et al., 2016c). The prevailing stress state is classified as close to transtensional ($S_{Hmax} \geq S_v > S_{hmin}$) with all three stress components inferred. This allows to estimate a preferential differential stress of 9 MPa which corresponds to a stress ratio of R_S=1.2 albeit uncertainties of up to 18MPa have to be considered in the stress components (Massiot et al., 2019). This information allows to use the herein estimated relations to derive a value for the stiffness contrast of R_E=0.8.

Further observations can be made for steeply dipping faults for example at the San Andreas Fault Observatory Drilling

275 (SAFOD) (Hickman and Zoback, 2004) or the Wenchuan fault drilling (Cui et al., 2014) (Table 4). At the SAFOD drilling site, a differential stress of 64 MPa (R_S=2.2) is expected with an angle between fault strike and S_{Hmax} orientation of 50° (Hickman and Zoback, 2004). The relations established in this paper predict that the observed stress rotation of approx. 30° requires a

Table 4. Observed stress rotations and associated parameters from different (scientific) boreholes which allow to derive the stiffness contrast.

Location	S$_1$-S$_3$ [MPa]	R$_S$	S$_{Hmax}$ vs. fault strike	Stress rotation	Fault dip angle	Reference	*R$_E$*
1. Taranaki Basin	6	1.2	0°	30°	90°	1	*0.8*
2. SAFOD	64	2.2	50°	30°	70° − 90°	2	*<0.1*
3. Wenchuan Fault	4 − 14	1.3 − 1.8	69°	<20°	70° − 90°	3	*<0.7*
4. KTB	175	2.4	0°	60°	70° − 80°	4	*<0.3*

1 Massiot et al. (2019), 2 Hickman and Zoback (2004), 3 Cui et al. (2014), 4 Brudy et al. (1997)

high stiffness contrast of R$_E$<0.1 (Table 4). This is consistent with (Zoback et al., 2011) observations in the San Andreas Fault Zone.

At the Wenchuan fault drilling project stress rotations of up to 20° are observed. A large angle between fault strike and S$_{Hmax}$ orientation and a small stress ratio (Cui et al., 2014) call for a rather moderate rock stiffness contrast of R$_E$<0.7 in order to explain the observed stress rotation angles (Table 4).

At the German Continental Deep Drilling site (KTB) 60° stress rotations are observed in unprecedented depths >7000m (Brudy et al., 1997). Considering the depth of observed stress rotation, the estimated stress magnitudes are high and so is the differential stress that is about 175 MPa and the stress ratio R$_S$=2.4 (Brudy et al., 1997). The small angle between fault strike and S$_{Hmax}$ orientation allows a 60° rotation to occur, even though R$_E$≤0.3 is required according to our generic approach.

The Taiwan Chelungpu Drilling Project (TCDP) drilled into the 30° dipping Chelungpu Fault which hosted the 1999 Chi-Chi earthquake (Hung et al., 2007; Lin et al., 2007). Stress rotations of up to 90° have been observed in the vicinity of the fault (Lin et al., 2007). Inferred differential stress and stress ratio, rock stiffness contrast and the observed stress rotation of 90° are well in agreement. However, the angle $\gamma = 90°$ between S$_{Hmax}$ and fault strike should prohibit any stress rotation at all. Interestingly, contrary to the other faults in Table 4, this one is not steeply dipping which may indicate the relevance of the intermediate principal stress component and the need to investigate the stress rotation in a full 3D modelling approach.

4.4 Limitations & Outlook

Most of our knowledge on the stress rotations at small scales are from the interpretation of borehole image logs. However, such rotations cannot be observed everywhere, mainly due to the uncertainties in borehole image log interpretation, in particular when it comes to the analysis of borehole breakouts (Azzola et al., 2019; Kingdon et al., 2016). Borehole breakouts are defined as a significant section of the borehole wall that spalls off (Aadnoy and Bell, 1998). In some cases, where breakouts are wide (i.e., opening angles of 15° - 30°) it is difficult to observe rotation <30° (Aadnoy and Bell, 1998). While rotation angles >30° can be observed easier using breakouts a higher certainty in observations is expected for drilling induced tensile fractures, which are usually described as thin (sub)vertical fractures, in vertical boreholes (Aadnoy and Bell, 1998). However, they are less frequently observed and harder to interpret and may be misinterpreted as incipient breakouts in some cases (Rajabi et al.,

2017b). In addition, borehole breakouts and/or drilling induced tensile fractures need to form in the first place both in the host rock and in the contrasting material in order to be able to detect a rotation at all. Thus, the detection of a stress rotation and even more so the estimation of the material contrast always is subject to uncertainties.

305   The presented approach in this study investigates elastic rock stiffness contrast in fault zones as the primary reason for stress rotations in a spatially homogeneous far-field stress state. In addition to these static stress rotations, temporal rotations of the principal stress axes can occur co-seismically or post-seismically due to natural seismicity (Hardebeck, 2017; Hardebeck and Okada, 2018; King et al., 1994; Nishiwaki et al., 2018). Further temporal back-and-forth rotation of the principal stress components have been observed (Martínez-Garzón et al., 2013, 2014) and related to reservoir operations such as injection of

310   fluids (Ziegler et al., 2017) as well as excavation works such as mining or tunnelling (Eberhardt, 2001; Ziegler et al., 2015). Stress rotation is not only observed at faults. It also occurs if lithological units are mechanically decoupled at a certain horizon due to a contrasting lithology. This also results in a perceived stress rotation in terms of different stress orientations above and below the respective horizon (Cornet and Röckel, 2012; Roth and Fleckenstein, 2001). These changes in rock properties e.g., in intrusions but also due to faults can cause massive changes in the S_{Hmax} orientation of up to 90° (Ahlers et al., 2018;

315   Cornet and Röckel, 2012; Rajabi et al., 2024; Reiter, 2021; Tingay et al., 2011). However, the different angles of S_{Hmax} could be rather inherited remnant stresses instead of local deviations due to material contrasts. In other cases, stress rotations cannot be attributed to a specific cause (Wang et al., 2023) or anisotropies are assumed (Sahara et al., 2014; Wang et al., 2022). As such, temporal stress rotations and decoupling effects are not covered by the presented work.

The failure of the generically derived relations to predict the expected stress rotation of 90° at the Chelungpu Fault (Table 4)

320   indicates a limitation of the approach. The behaviour of any faults that have a significant deviation from a vertical to subvertical dip apparently do not follow the proposed scheme. This is expected to be a result of its limitation to two dimensions even though the generically modelled fault strike could also represent the dip. That shows the influence of the intermediate principal stress which cannot be investigated in a 2D model. Furthermore, the observed rotation of the S_{Hmax} orientation is only a part of the actual rotation which likely concerns all principal stress component's magnitude and orientation, as observed by the analysis

325   of focal mechanism solutions e.g. by Martínez-Garzón et al. (2013, 2014). This indicates the necessity to extend the presented approach to the full 3D stress tensor. In particular, this includes the necessity to investigate the influence of the intermediate principal stress component S_2 and its relation to S_1 and S_3. This should be the aim of future studies as it is well beyond the scope of this work.

5   Conclusions

330   We investigate the relationship between stress rotation in a fault core influenced by 1) a variable rock stiffness contrast compared to the host rock, 2) the stress ratio of the far field, and 3) the far field stress orientation with regards to the strike of the fault. We use a 2D plane strain model that shows in a sensitivity study that stress rotation is promoted by a low stress ratio and a low angle between the far field stress orientation and the fault strike. A high stiffness contrast further increases the stress rotation angle. No stress rotation is possible for faults that are striking perpendicular to the maximum principal stress

335 orientation while faults parallel to the maximum principal stress orientation experience either no stress rotation or a 90° stress rotation, dependent on the stress ratio and the rock stiffness contrast within the fault core. The established relations agree with observations from various scientific boreholes worldwide. However, they are only valid for steeply dipping faults where the intermediate principal stress component S_2 only has a minor effect. A fully 3D investigation of the established relations including the effect of S_2 should be addressed in future research.

340 *Data availability.* All modelling results are available in the supporting material.

Appendix A: Mesh convergence

The discretization and thus the element size has an effect on model results. In order to prevent interpretation of results influenced by the discretization, a mesh convergence check is performed. The same model geometry is discretized with different element sizes and therefore a different total number of elements. Then, the different variations are solved and the results are

345 compared, in this case the modelled stress rotation angle.

Herein, two different variations in discretization are investigated. First, the absolute number of elements used to discretize the model. Four different realizations are tested, namely 300, 3,000, 170,000, and 700,000 elements. Second, the number of elements that are used to represent the fault normal to the fault strike are varied (Figure A1). We tested seven different scenarios, namely with 1, 3, 5, 7, 10, 15, and 20 elements normal to the fault strike. All combinations of total numbers of elements and

350 fault elements were combined, so that in total 28 different discretization scenarios were tested.

To test the influence of the discretization on the results, the discretizations were compared using an identical set of parameters. The reference set of parameters from Figure 3a was chosen. This means an angle $\gamma = 15°$ between the strike of the fault and the far field stress (S_1), a stiffness contrast R_E=0.4 (16 GPa fault, 40 GPa host rock), and a principal stress ratio R_S=1.4 (S_1 = 35 MPa, S_2 = 25 MPa, S_1-S_2 = 10 MPa). This set of parameters was used on all 28 different discretization scenarios.

355 The resulting stress rotation angle that is only dependent on the discretization is shown in Figure A2. The total number of elements in the tested range does not show any impact on the stress rotation angle. However, the number of elements used for fault representation normal to the fault strike significantly influence the results. This influence, however, is limited to a fault represented by <3 elements normal to the strike (Figure A2). This effect is observed independent of the total number of elements. These results indicate that the discretization approach realised in this study (20 elements normal to fault strike,

360 approx. 170,000 elements in total, red dot in Figure A2) is very well suited to model the stress rotation angle. An influence of the discretization on the results can be ruled out.
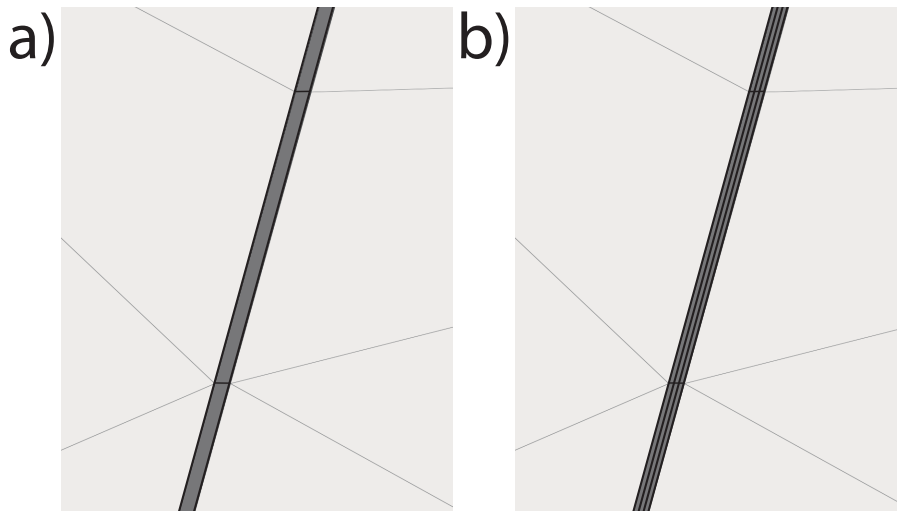
Figure A1. Examples of fault discretization. While the absolute number of elements remains approximately the same, the number of elements used for fault discretization varies. a) A single element is used to discretize the fault. b) Three elements are used normal to fault strike to represent the fault.
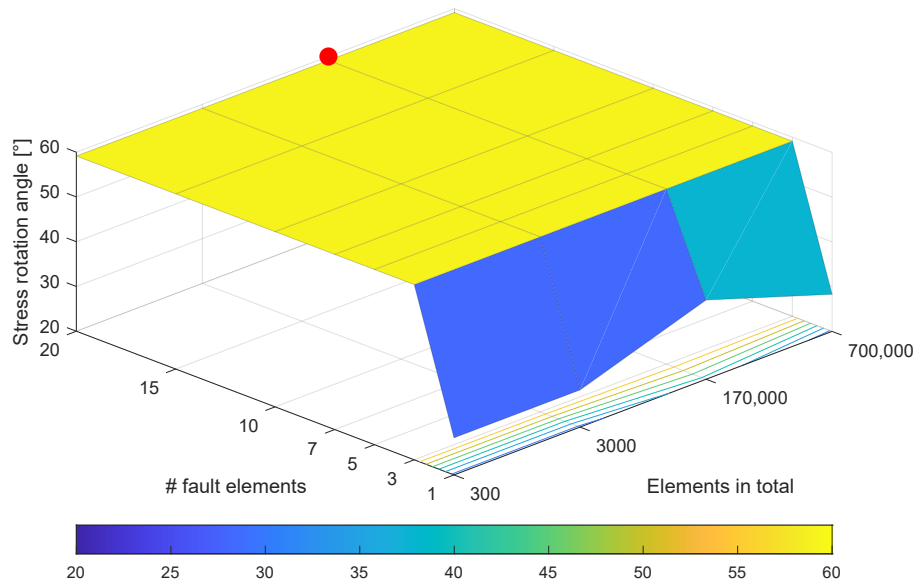

Figure A2. Stress rotation in dependence of different discretizations. The total number of elemenents (y-axis) and the number of elements used to represent the fault normal to its strike (x-axis) are put into relation to the modelled stress rotation angle (z-axis). The approximate mesh resolution used for this study is indicated by the red dot. The tested parameters are the same as in Figure 3a.

22

References

Aadnoy, B. S. and Bell, J. S.: Classification Of Drilling-induced Fractures And Their Relationship To In-situ Stress Directions, The Log Analyst, 39, 1998.

Ahlers, S., Hergert, T., and Henk, A.: Numerical Modelling of Salt-Related Stress Decoupling in Sedimentary Basins–Motivated by Observational Data from the North German Basin, Geosciences 2019, Vol. 9, Page 19, 9, 19, https://doi.org/10.3390/GEOSCIENCES9010019, 2018.

Ahlers, S., Röckel, L., Hergert, T., Reiter, K., Heidbach, O., Henk, A., Müller, B., Morawietz, S., Scheck-Wenderoth, M., and Anikiev, D.: The crustal stress field of Germany: a refined prediction, Geothermal Energy, 10, 10, https://doi.org/10.1186/s40517-022-00222-6, 2022.

Azzola, J., Valley, B., Schmittbuhl, J., and Genter, A.: Stress characterization and temporal evolution of borehole failure at the Rittershoffen geothermal project, Solid Earth, 10, 1155–1180, https://doi.org/10.5194/se-10-1155-2019, 2019.

Barton, C. A. and Zoback, M. D.: Stress perturbations associated with active faults penetrated by boreholes: Possible evidence for near-complete stress drop and a new technique for stress magnitude measurement, Journal of Geophysical Research: Solid Earth, 99, 9373–9390, https://doi.org/10.1029/93JB03359, 1994.

Barton, C. A., Zoback, M. D., and Moos, D.: Fluid flow along potentially active faults in crystalline rock, Geology, 23, 683, https://doi.org/10.1130/0091-7613(1995)023<0683:FFAPAF>2.3.CO;2, 1995.

Bell, J. and Gough, D.: Northeast-southwest compressive stress in Alberta evidence from oil wells, Earth and Planetary Science Letters, 45, 475–482, https://doi.org/10.1016/0012-821X(79)90146-8, 1979.

Brodsky, E. E., Saffer, D., Fulton, P., Chester, F., Conin, M., Huffman, K., Moore, J. C., and Wu, H.: The postearthquake stress state on the Tohoku megathrust as constrained by reanalysis of the JFAST breakout data, Geophysical Research Letters, 44, 8294–8302, https://doi.org/10.1002/2017GL074027, 2017.

Brudy, M., Zoback, M. D., Fuchs, K., Rummel, F., and Baumgaertner, J.: Estimation of the complete stress tensor to 8 km depth in the KTB scientific drill holes' Implications for crustal strength, JOURNAL OF GEOPHYSICAL RESEARCH, 102, 453–471, https://doi.org/10.1029/96JB02942, 1997.

Cai, W., Zhu, H., and Liang, W.: Three-dimensional stress rotation and control mechanism of deep tunneling incorporating generalized Zhang–Zhu strength-based forward analysis, Engineering Geology, 308, 106 806, https://doi.org/10.1016/j.enggeo.2022.106806, 2022.

Cappa, F. and Rutqvist, J.: Impact of CO2 geological sequestration on the nucleation of earthquakes, Geophysical Research Letters, 38, https://doi.org/https://doi.org/10.1029/2011GL048487, 2011.

Casey, M.: Mechanics of shear zones in isotropic dilatant materials, Journal of Structural Geology, 2, 143–147, https://doi.org/10.1016/0191-8141(80)90044-9, 1980.

Catalli, F., Meier, M. A., and Wiemer, S.: The role of Coulomb stress changes for injection-induced seismicity: The Basel enhanced geothermal system, Geophysical Research Letters, 40, 72–77, https://doi.org/10.1029/2012GL054147, 2013.

Childs, C., Manzocchi, T., Walsh, J. J., Bonson, C. G., Nicol, A., and Schöpfer, M. P.: A geometric model of fault zone and fault rock thickness variations, Journal of Structural Geology, 31, 117–127, https://doi.org/https://doi.org/10.1016/j.jsg.2008.08.009, 2009.

Clavijo, S. P., Dash, A., Baby, G., Alafifi, A. M., and Finkbeiner, T.: Modeling principal stress orientations in the Arabian Plate using plate velocities, Geological Society, London, Special Publications, 546, https://doi.org/10.1144/SP546-2022-327, 2024.

Collettini, C., Niemeijer, A., Viti, C., and Marone, C.: Fault zone fabric and fault weakness, Nature, 462, 907–910, 2009.

Cornet, F. H. and Röckel, T.: Vertical stress profiles and the significance of "stress decoupling", Tectonophysics, 581, 193–205, https://doi.org/10.1016/J.TECTO.2012.01.020, 2012.

Cui, J., Lin, W., Wang, L., Gao, L., Huang, Y., Wang, W., Sun, D., Li, Z., Zhou, C., Qian, H., Peng, H., Xia, K., and Li, K.: Determination of three-dimensional in situ stresses by anelastic strain recovery in Wenchuan Earthquake Fault Scientific Drilling Project Hole-1 (WFSD-1), Tectonophysics, 619-620, 123–132, https://doi.org/10.1016/j.tecto.2013.09.013, 2014.

Dart, R. and Swolfs, H.: Subparallel faults and horizontal-stress orientations: an evaluation of in-situ stresses inferred from elliptical wellbore enlargements, pp. 519–529, Elsevier, https://doi.org/10.1016/B978-0-444-88607-1.50041-3, 1992.

Eberhardt, E.: Numerical modelling of three-dimension stress rotation ahead of an advancing tunnel face, International Journal of Rock Mechanics and Mining Sciences, 38, 499–518, https://doi.org/10.1016/S1365-1609(01)00017-X, 2001.

Engelder, T.: Stress Regimes in the Lithosphere, Princeton University Press, ISBN 9781400863150, https://doi.org/10.1515/9781400863150, 1992.

Engelder, T.: Deviatoric stressitis: A virus infecting the Earth science community, Eos, Transactions American Geophysical Union, 75, 209–212, https://doi.org/10.1029/94EO00885, 1994.

Faulkner, D. R., Mitchell, T. M., Healy, D., and Heap, M. J.: Slip on 'weak' faults by the rotation of regional stress in the fracture damage zone, Nature, 444, 922–925, https://doi.org/10.1038/nature05353, 2006.

Faulkner, D. R., Jackson, C. A., Lunn, R. J., Schlische, R. W., Shipton, Z. K., Wibberley, C. A., and Withjack, M. O.: A review of recent developments concerning the structure, mechanics and fluid flow properties of fault zones, Journal of Structural Geology, 32, 1557–1575, https://doi.org/10.1016/J.JSG.2010.06.009, 2010.

Freymark, J., Bott, J., Cacace, M., Ziegler, M. O., and Scheck-Wenderoth, M.: Influence of the Main Border Faults on the 3D Hydraulic Field of the Central Upper Rhine Graben, Geofluids, 2019, https://doi.org/10.1155/2019/7520714, 2019.

Gabrielsen, R. H., Braathen, A., Kjemperud, M., and Valdresbråten, M. L. R.: The geometry and dimensions of fault-core lenses, Geological Society, London, Special Publications, 439, 249–269, https://doi.org/10.1144/SP439.4, 2017.

Gaucher, E., Schoenball, M., Heidbach, O., Zang, A., Fokker, P. A., Wees, J. D. V., and Kohl, T.: Induced seismicity in geothermal reservoirs: A review of forecasting approaches, https://doi.org/10.1016/j.rser.2015.08.026, 2015.

Gilmore, K. A., Sahu, C. K., Benham, G. P., Neufeld, J. A., and Bickle, M. J.: Leakage dynamics of fault zones: experimental and analytical study with application to CO2 storage, Journal of Fluid Mechanics, 931, A31, https://doi.org/10.1017/JFM.2021.970, 2022.

Gradmann, S., Olesen, O., Keiding, M., and Maystrenko, Y.: The 3D stress field of Nordland, northern Norway - insights from numerical modelling, Geological Society, London, Special Publications, 546, https://doi.org/10.1144/SP546-2023-163, 2024.

Haimson, B., Lin, W., Oku, H., Hung, J. H., and Song, S. R.: Integrating borehole-breakout dimensions, strength criteria, and leak-off test results, to constrain the state of stress across the Chelungpu Fault, Taiwan, Tectonophysics, 482, 65–72, https://doi.org/10.1016/J.TECTO.2009.05.016, 2010.

Han, C., Huang, Z., Xu, M., Wang, L., Mi, N., Yu, D., and Li, H.: Focal mechanism and stress field in the northeastern Tibetan Plateau: insight into layered crustal deformations, Geophysical Journal International, 218, 2066–2078, https://doi.org/10.1093/gji/ggz267, 2019.

Hardebeck, J. L.: The spatial distribution of earthquake stress rotations following large subduction zone earthquakes, Earth, Planets and Space, 69, https://doi.org/10.1186/s40623-017-0654-y, 2017.

Hardebeck, J. L. and Okada, T.: Temporal Stress Changes Caused by Earthquakes: A Review, https://doi.org/10.1002/2017JB014617, 2018.

Healy, D. and Hicks, S. P.: De-risking the energy transition by quantifying the uncertainties in fault stability, Solid Earth, 13, 15–39, https://doi.org/10.5194/se-13-15-2022, 2022.

Heidbach, O., Rajabi, M., Cui, X., Fuchs, K., Müller, B., Reinecker, J., Reiter, K., Tingay, M., Wenzel, F., Xie, F., Ziegler, M. O., Zoback, M.-L., and Zoback, M.: The World Stress Map database release 2016: Crustal stress pattern across scales, Tectonophysics, 744, 484–498, https://doi.org/10.1016/j.tecto.2018.07.007, 2018.

Henk, A.: Chapter 4 - Numerical modelling of faults, pp. 147–165, Elsevier, ISBN 978-0-12-815985-9, https://doi.org/https://doi.org/10.1016/B978-0-12-815985-9.00004-7, 2020.

Hergert, T., Heidbach, O., Reiter, K., Giger, S. B., and Marschall, P.: Stress field sensitivity analysis in a sedimentary sequence of the Alpine foreland, northern Switzerland, Solid Earth, 6, 533–552, https://doi.org/10.5194/se-6-533-2015, 2015.

Hickman, S. and Zoback, M.: Stress orientations and magnitudes in the SAFOD pilot hole, Geophysical Research Letters, 31, https://doi.org/10.1029/2004GL020043, 2004.

Holdsworth, R. E.: Weak Faults–Rotten Cores, Science, 303, 181–182, https://doi.org/10.1126/science.1092491, 2004.

Holdsworth, R. E., Diggelen, E. W. E. V., Spiers, C. J., Bresser, J. H. P. D., Walker, R. J., and Bowen, L.: Fault rocks from the SAFOD core samples: Implications for weakening at shallow depths along the San Andreas Fault, California, Journal of Structural Geology, https://doi.org/10.1016/j.jsg.2010.11.010, 2010.

Homberg, C., Hu, J. C., Angelier, J., Bergerat, F., and Lacombe, O.: Characterization of stress perturbations near major fault zones: insights from 2-D distinct-element numerical modelling and field studies (Jura mountains), Journal of Structural Geology, 19, 703–718, https://doi.org/10.1016/S0191-8141(96)00104-6, 1997.

Hung, J.-H., Ma, K.-F., Wang, C.-Y., Ito, H., Lin, W., and Yeh, E.-C.: Subsurface structure, physical properties, fault-zone characteristics and stress state in scientific drill holes of Taiwan Chelungpu Fault Drilling Project, Tectonophysics, 466, 307–321, https://doi.org/10.1016/j.tecto.2007.11.014, 2007.

Isaacs, A. J., Evans, J. P., Kolesar, P. T., and Nohara, T.: Composition, microstructures, and petrophysics of the Mozumi fault, Japan: In situ analyses of fault zone properties and structure in sedimentary rocks from shallow crustal levels, Journal of Geophysical Research: Solid Earth, 113, https://doi.org/10.1029/2007JB005314, 2008.

King, C. P., Stein, R. O. S. S. S., and Lin, J.: Static Stress Changes and the Triggering of Earthquakes, Bulletin of the Seismological Society of America, 84, 935–953, https://doi.org/10.1785/BSSA0840030935, 1994.

Kingdon, A., Fellgett, M. W., and Williams, J. D.: Use of borehole imaging to improve understanding of the in-situ stress orientation of Central and Northern England and its implications for unconventional hydrocarbon resources, Marine and Petroleum Geology, 73, 1–20, https://doi.org/10.1016/j.marpetgeo.2016.02.012, 2016.

Kirsch, E.: Die Theorie der Elastizität und die Bedürfnisse der Festigkeitslehre, Zeitschrift des Vereines deutscher Ingenieure, 42, 1898.

Konrad, F., Savvatis, A., Degen, D., Wellmann, F., Einsiedl, F., and Zosseder, K.: Productivity enhancement of geothermal wells through fault zones: Efficient numerical evaluation of a parameter space for the Upper Jurassic aquifer of the North Alpine Foreland Basin, Geothermics, 95, 102 119, https://doi.org/10.1016/J.GEOTHERMICS.2021.102119, 2021.

Konstantinou, K. I., Mouslopoulou, V., Liang, W. T., Heidbach, O., Oncken, O., and Suppe, J.: Present-day crustal stress field in Greece inferred from regional-scale damped inversion of earthquake focal mechanisms, Journal of Geophysical Research: Solid Earth, 122, 506–523, https://doi.org/10.1002/2016JB013272, 2017.

Konstantinovskaya, E., Malo, M., and Castillo, D.: Present-day stress analysis of the St. Lawrence Lowlands sedimentary basin (Canada) and implications for caprock integrity during CO2 injection operations, Tectonophysics, 518-521, 119–137, https://doi.org/10.1016/j.tecto.2011.11.022, 2012.

Levi, N., Habermueller, M., Exner, U., Piani, E., Wiesmayr, G., and Decker, K.: The stress field in the frontal part of the Eastern Alps (Austria) from borehole image log data, Tectonophysics, 769, 228 175, https://doi.org/10.1016/J.TECTO.2019.228175, 2019.

Li, H., Wang, H., Xu, Z., Si, J., Pei, J., Li, T., Huang, Y., Song, S.-R., Kuo, L.-W., Sun, Z., Chevalier, M.-L., and Liu, D.: Characteristics of the fault-related rocks, fault zones and the principal slip zone in the Wenchuan Earthquake Fault Scientific Drilling Project Hole-1 (WFSD-1), Tectonophysics, https://doi.org/10.1016/j.tecto.2012.08.021, 2012.

Li, P., Cai, M., Gorjian, M., Ren, F., Xi, X., and Wang, P.: Interaction between in situ stress states and tectonic faults: A comment, International Journal of Minerals, Metallurgy and Materials, 30, 1227–1243, https://doi.org/10.1007/S12613-023-2607-8/METRICS, 2023.

Lin, W., Yeh, E.-C., Ito, H., Hirono, T., Soh, W., Wang, C.-Y., Ma, K.-F., Hung, J.-H., and Song, S.-R.: Preliminary Results of Stress Measurement Using Drill Cores of TCDP Hole-A: an Application of Anelastic Strain Recovery Method to Three-Dimensional In-Situ Stress Determination, Terr. Atmos. Ocean. Sci, 18, 380, https://doi.org/10.3319/TAO.2007.18.2.379(TCDP), 2007.

Lin, W., Yeh, E.-C., Hung, J.-H., Haimson, B., and Hirono, T.: Localized rotation of principal stress around faults and fractures determined from borehole breakouts in hole B of the Taiwan Chelungpu-fault Drilling Project (TCDP), Tectonophysics, 482, 82–91, https://doi.org/10.1016/j.tecto.2009.06.020, 2010.

Lockner, D. A., Tanaka, H., Ito, H., Ikeda, R., Omura, K., and Naka, H.: Geometry of the Nojima fault at Nojima-Hirabayashi, Japan - I. A simple damage structure inferred from borehole core permeability, Pure and Applied Geophysics, 166, 1649–1667, https://doi.org/10.1007/S00024-009-0515-0/METRICS, 2009.

Long, J. C. and Ewing, R. C.: YUCCA MOUNTAIN: Earth-Science Issues at a Geologic Repository for High-Level Nuclear Waste, Annual Review of Earth and Planetary Sciences, 32, 363–401, https://doi.org/10.1146/annurev.earth.32.092203.122444, 2004.

Martínez-Garzón, P., Bohnhoff, M., Kwiatek, G., and Dresen, G.: Stress tensor changes related to fluid injection at the Geysers geothermal field, California, Geophysical Research Letters, 40, 2596–2601, https://doi.org/10.1002/grl.50438, 2013.

Martínez-Garzón, P., Kwiatek, G., Sone, H., Bohnhoff, M., Dresen, G., and Hartline, C.: Spatiotemporal changes, faulting regimes, and source parameters of induced seismicity: A case study from the Geysers geothermal field, Journal of Geophysical Research: Solid Earth, 119, 8378–8396, https://doi.org/10.1002/2014JB011385, 2014.

Massiot, C., Seebeck, H., Nicol, A., McNamara, D. D., Lawrence, M. J., Griffin, A. G., Thrasher, G. P., O'Brien, G., and Viskovic, G. P. D.: Effects of regional and local stresses on fault slip tendency in the southern Taranaki Basin, New Zealand, Marine and Petroleum Geology, 107, 467–483, https://doi.org/10.1016/J.MARPETGEO.2019.05.030, 2019.

Morris, A., Ferrill, D. A., and Henderson, D. B.: Slip-tendency analysis and fault reactivation, Geology, 24, 275, https://doi.org/10.1130/0091-7613(1996)024<0275:STAAFR>2.3.CO;2, 1996.

Müller, B., Schilling, F., Röckel, T., and Heidbach, O.: Induced Seismicity in Reservoirs: Stress Makes the Difference Induzierte, Erdöl Erdgas Kohle, https://doi.org/10.19225/180106, 2018.

Nabavi, S. T., Alavi, S. A., Mohammadi, S., and Ghassemi, M. R.: Mechanical evolution of transpression zones affected by fault interactions: Insights from 3D elasto-plastic finite element models, Journal of Structural Geology, 106, 19–40, https://doi.org/https://doi.org/10.1016/j.jsg.2017.11.003, 2018.

Niederhuber, T., Kruszewski, M., Röckel, T., Rische, M., Alber, M., and Müller, B.: Stress orientations from hydraulic fracturing tests in the Ruhr area in comparison to stress orientations from borehole observations and earthquake focal mechanisms, Zeitschrift der Deutschen Gesellschaft für Geowissenschaften, 173, 625–635, https://doi.org/10.1127/zdgg/2022/0352, 2023.

Nishiwaki, T., Lin, A., and Lin, W.: Recovery of Stress During the Interseismic Period Around the Seismogenic Fault of the 1995 Mw 6.9 Kobe Earthquake, Japan, Geophysical Research Letters, 45, 12,814–12,820, https://doi.org/https://doi.org/10.1029/2018GL079317, 2018.

Ptáček, J., Konicek, P., Staš, L., Waclawik, P., and Kukutsch, R.: Rotation of principal axes and changes of stress due to mine-induced stresses, Canadian Geotechnical Journal, 52, 1440–1447, https://doi.org/10.1139/cgj-2014-0364, 2015.

Rajabi, M., Tingay, M., and Heidbach, O.: The present-day state of tectonic stress in the Darling Basin, Australia: Implications for exploration and production, Marine and Petroleum Geology, 77, 776–790, https://doi.org/10.1016/j.marpetgeo.2016.07.021, 2016a.

Rajabi, M., Tingay, M., and Heidbach, O.: The present-day stress field of New South Wales, Australia, Australian Journal of Earth Sciences, 63, 1–21, https://doi.org/10.1080/08120099.2016.1135821, 2016b.

Rajabi, M., Ziegler, M. O., Tingay, M., Heidbach, O., and Reynolds, S.: Contemporary tectonic stress pattern of the Taranaki Basin, New Zealand, Journal of Geophysical Research: Solid Earth, 121, 6053–6070, https://doi.org/10.1002/2016JB013178, 2016c.

Rajabi, M., Tingay, M., Heidbach, O., Hillis, R., and Reynolds, S.: The present-day stress field of Australia, https://doi.org/10.1016/j.earscirev.2017.04.003, 2017a.

Rajabi, M., Tingay, M., King, R., and Heidbach, O.: Present-day stress orientation in the Clarence-Moreton Basin of New South Wales, Australia: a new high density dataset reveals local stress rotations, Basin Research, 29, 622–640, https://doi.org/10.1111/bre.12175, 2017b.

Rajabi, M., Esterle, J., Heidbach, O., Travassos, D., and Fumo, S.: Characterising the contemporary stress orientations near an active continental rifting zone: A case study from the Moatize Basin, central Mozambique, Basin Research, 34, 1292–1313, https://doi.org/10.1111/bre.12660, 2022.

Rajabi, M., Ziegler, M., Heidbach, O., Mukherjee, S., and Esterle, J.: Contribution of mine borehole data toward high-resolution stress mapping: An example from northern Bowen Basin, Australia, International Journal of Rock Mechanics and Mining Sciences, 173, 105 630, https://doi.org/10.1016/j.ijrmms.2023.105630, 2024.

Reinecker, J., Tingay, M., Müller, B., and Heidbach, O.: Present-day stress orientation in the Molasse Basin, Tectonophysics, 482, 129–138, https://doi.org/10.1016/j.tecto.2009.07.021, 2010.

Reiter, K.: Stress rotation – impact and interaction of rock stiffness and faults, Solid Earth, 12, 1287–1307, https://doi.org/10.5194/se-12-1287-2021, 2021.

Reiter, K., Heidbach, O., Schmitt, D., Haug, K., Ziegler, M. O., and Moeck, I.: A revised crustal stress orientation database for Canada, Tectonophysics, 636, 111–124, https://doi.org/10.1016/j.tecto.2014.08.006, 2014.

Reiter, K., Heidbach, O., and Ziegler, M. O.: Impact of faults on the remote stress state, Solid Earth, 15, 305–327, https://doi.org/10.5194/se-15-305-2024, 2024.

Roth, F. and Fleckenstein, P.: Stress orientations found in north-east Germany differ from the West European trend, Terra Nova, 13, 289–296, https://doi.org/10.1046/J.1365-3121.2001.00357.X, 2001.

Röckel, L., Ahlers, S., Müller, B., Reiter, K., Heidbach, O., Henk, A., Hergert, T., and Schilling, F.: The analysis of slip tendency of major tectonic faults in Germany, Solid Earth, 13, 1087–1105, https://doi.org/10.5194/se-13-1087-2022, 2022.

Sahara, D. P., Schoenball, M., Kohl, T., and Müller, B. I.: Impact of fracture networks on borehole breakout heterogeneities in crystalline rock, International Journal of Rock Mechanics and Mining Sciences, 71, 301–309, https://doi.org/10.1016/j.ijrmms.2014.07.001, 2014.

Schoenball, M., Dorbath, L., Gaucher, E., Wellmann, J. F., and Kohl, T.: Change of stress regime during geothermal reservoir stimulation, Geophysical Research Letters, 41, 1163–1170, https://doi.org/10.1002/2013GL058514, 2014.

Schoenball, M., Walsh, F. R., Weingarten, M., and Ellsworth, W. L.: How faults wake up: The Guthrie-Langston, Oklahoma earthquakes, The Leading Edge, 37, 100–106, https://doi.org/10.1190/tle37020100.1, 2018.

Seithel, R., Steiner, U., Müller, B., Hecht, C., and Kohl, T.: Local stress anomaly in the Bavarian Molasse Basin, Geothermal Energy, 3, https://doi.org/10.1186/s40517-014-0023-z, 2015.

Seithel, R., Gaucher, E., Mueller, B., Steiner, U., and Kohl, T.: Probability of fault reactivation in the Bavarian Molasse Basin, Geothermics, 82, 81–90, https://doi.org/10.1016/j.geothermics.2019.06.004, 2019.

Shamir, G. and Zoback, M. D.: Stress orientation profile to 3.5 km depth near the San Andreas Fault at Cajon Pass, California, Journal of Geophysical Research: Solid Earth, 97, 5059–5080, https://doi.org/10.1029/91JB02959, 1992.

Siler, D. L.: Structural discontinuities and their control on hydrothermal systems in the Great Basin, USA, Geoenergy, 1, https://doi.org/10.1144/geoenergy2023-009, 2023.

Snee, J. E. L. and Zoback, M. D.: State of stress in the Permian Basin, Texas and New Mexico: Implications for induced seismicity, The Leading Edge, 37, 127–134, https://doi.org/10.1190/TLE37020127.1, 2018.

Sonder, L. J.: EFFECTS OF DENSITY CONTRASTS ON THE ORIENTATION OF STRESSES IN THE LITHOSPHERE: RELATION TO PRINCIPAL STRESS DIRECTIONS IN THE TRANSVERSE RANGES, CALIFORNIA, 1990.

Spann, H., Müller, B., and Fuchs, K.: Interpretation of anomalies in observed stress data at the central graben (north sea) — numerical and analytical approach, Soil Dynamics and Earthquake Engineering, 13, 1–11, https://doi.org/10.1016/0267-7261(94)90036-1, 1994.

Talukdar, M., Sone, H., and Kuo, L.: Lithology and Fault-Related Stress Variations Along the TCDP Boreholes: The Stress State Before and After the 1999 Chi-Chi Earthquake, Journal of Geophysical Research: Solid Earth, 127, https://doi.org/10.1029/2021JB023290, 2022.

Tingay, M., Bentham, P., de Feyter, A., and Kellner, A.: Present-day stress-field rotations associated with evaporites in the offshore Nile Delta, Bulletin of the Geological Society of America, 123, 1171–1180, https://doi.org/10.1130/B30185.1, 2011.

Treffeisen, T. and Henk, A.: Representation of faults in reservoir-scale geomechanical finite element models – A comparison of different modelling approaches, Journal of Structural Geology, 131, 103 931, https://doi.org/10.1016/j.jsg.2019.103931, 2020.

Vadacca, L., Rossi, D., Scotti, A., and Buttinelli, M.: Slip Tendency Analysis, Fault Reactivation Potential and Induced Seismicity in the Val d'Agri Oilfield (Italy), Journal of Geophysical Research: Solid Earth, 126, https://doi.org/10.1029/2019JB019185, 2021.

van Wees, J.-D., Osinga, S., Thienen-Visser, K. V., and Fokker, P. A.: Reservoir creep and induced seismicity: inferences from geomechanical modeling of gas depletion in the Groningen field, Geophysical Journal International, 212, 1487–1497, https://doi.org/10.1093/gji/ggx452, 2018.

Wang, W., Schmitt, D. R., and Li, W.: A program to forward model the failure pattern around the wellbore in elastic and strength anisotropic rock formations, International Journal of Rock Mechanics and Mining Sciences, 151, 105 035, https://doi.org/10.1016/j.ijrmms.2022.105035, 2022.

Wang, W., Schmitt, D. R., and Chan, J.: Heterogeneity Versus Anisotropy and the State of Stress in Stable Cratons: Observations From a Deep Borehole in Northeastern Alberta, Canada, Journal of Geophysical Research: Solid Earth, 128, https://doi.org/10.1029/2022JB025287, 2023.

Wees, J. D. V., Orlic, B., Eijs, R. V., Zijl, W., Jongerius, P., Schreppers, G. J., Hendriks, M., and Cornu, . T.: Integrated 3D geomechanical modelling for deep subsurface deformation: a case study of tectonic and human-induced deformation in the eastern Netherlands, http://sp.lyellcollection.org/, 2003.

Williams, J. N., Toy, V. G., Massiot, E., Mcnamara, D. D., and Wang, T.: Damaged beyond repair? Characterising the damage zone of a fault late in its interseismic cycle, the Alpine Fault, New Zealand, Journal of Structural Geology, https://doi.org/10.1016/j.jsg.2016.07.006, 2016.

Worum, G., van Wees, J.-D., Bada, G., van Balen, R. T., Cloetingh, S., and Pagnier, H.: Slip tendency analysis as a tool to constrain fault reactivation: A numerical approach applied to three-dimensional fault models in the Roer Valley rift system (southeast Netherlands), Journal of Geophysical Research: Solid Earth, 109, https://doi.org/10.1029/2003JB002586, 2004.

Xing, H., Makinouchi, A., and Mora, P.: Finite element modeling of interacting fault systems, Physics of the Earth and Planetary Interiors, 163, 106–121, https://doi.org/10.1016/j.pepi.2007.05.006, 2007.

Yale, D. P.: Fault and stress magnitude controls on variations in the orientation of *in situ* stress, Geological Society, London, Special Publications, 209, 55–64, https://doi.org/10.1144/GSL.SP.2003.209.01.06, 2003.

Yamada, Y. and Shibanuma, J.: Small-scale stress fluctuations in borehole breakouts and their implication in identifying potential active faults around the seismogenic megasplay fault, Nankai Trough, SW Japan, Earth, Planets and Space, 67, 17, https://doi.org/10.1186/s40623-014-0176-9, 2015.

Zhang, S., Ma, X., Bröker, K., van Limborgh, R., Wenning, Q., Hertrich, M., and Giardini, D.: Fault Zone Spatial Stress Variations in a Granitic Rock Mass: Revealed by Breakouts Within an Array of Boreholes, Journal of Geophysical Research: Solid Earth, 128, https://doi.org/10.1029/2023JB026477, 2023.

Ziegler, M. O.: Rock Properties and Modelled Stress State Uncertainties: A Study of Variability and Dependence, Rock Mechanics and Rock Engineering, https://doi.org/10.1007/s00603-022-02879-8, 2022.

Ziegler, M. O., Reiter, K., Heidbach, O., Zang, A., Kwiatek, G., Stromeyer, D., Dahm, T., Dresen, G., and Hofmann, G.: Mining-Induced Stress Transfer and Its Relation to a Mw 1.9 Seismic Event in an Ultra-deep South African Gold Mine, Pure and Applied Geophysics, 172, 2557–2570, https://doi.org/10.1007/s00024-015-1033-x, 2015.

Ziegler, M. O., Heidbach, O., Reinecker, J., Przybycin, A. M., and Scheck-Wenderoth, M.: A multi-stage 3-D stress field modelling approach exemplified in the Bavarian Molasse Basin, Solid Earth, 7, 1365–1382, https://doi.org/10.5194/se-7-1365-2016, 2016a.

Ziegler, M. O., Heidbach, O., Reinecker, J., Przybycin, A. M., and Scheck-Wenderoth, M.: Corrigendum to "A multi-stage 3-D stress field modelling approach exemplified in the Bavarian Molasse Basin" published in Solid Earth, 7, 1365–1382, 2016, Solid Earth, 7, 1365–1382, https://doi.org/10.5194/se-7-1365-2016-corrigendum, 2016b.

Ziegler, M. O., Rajabi, M., Heidbach, O., Hersir, G. P., Ágústsson, K., Árnadóttir, S., and Zang, A.: The stress pattern of Iceland, Tectonophysics, 674, 101–113, https://doi.org/10.1016/j.tecto.2016.02.008, 2016c.

Ziegler, M. O., Heidbach, O., Zang, A., Martínez-Garzón, P., and Bohnhoff, M.: Estimation of the differential stress from the stress rotation angle in low permeable rock, Geophysical Research Letters, 44, 6761–6770, https://doi.org/10.1002/2017GL073598, 2017.

Ziegler, M. O., Heidbach, O., Morawietz, S., and Wang, Y.: Manual of the Matlab Script FAST Calibration v2.4, https://doi.org/10.48440/wsm.2023.002, 2023.

Zoback, M., Hickman, S., Ellsworth, W., and the SAFOD Science Team: Scientific Drilling Into the San Andreas Fault Zone – An Overview of SAFOD's First Five Years, Scientific Drilling, 11, 14–28, https://doi.org/10.2204/iodp.sd.11.02.2011, 2011.

Zoback, M. L.: First- and second-order patterns of stress in the lithosphere: The World Stress Map Project, Journal of Geophysical Research: Solid Earth, 97, 11 703–11 728, https://doi.org/10.1029/92JB00132, 1992.